J Solid State Electrochem (2017) 21:145–152
DOI 10.1007/s10008-016-3345-x

ORIGINAL PAPER

$LiMO_2$@Li_2MnO_3 positive-electrode material for high energy density lithium ion batteries

Mohammed Adnan Mezaal[1,2] · Limin Qu[1] · Guanghua Li[1,3] · Wei Liu[1] · Xiaoyuan Zhao[1] · Ke Zhang[1] · Rui Zhang[1] · Lixu Lei[1]

Received: 31 May 2016 / Revised: 20 July 2016 / Accepted: 22 July 2016 / Published online: 9 August 2016

Abstract $Li[Ni_{1/3}Co_{1/3}Mn_{1/3}]O_2$ (NCM 111) is a promising alternative to $LiCoO_2$, as it is less expensive, more structurally stable, and has better safety characteristics. However, its capacity of 155 mAh g^{-1} is quite low, and cycling at potentials above 4.5 V leads to rapid capacity deterioration. Here, we report a successful synthesis of lithium-rich layered oxides (LLOs) with a core of $LiMO_2$ (*R*-3m, M = Ni, Co) and a shell of Li_2MnO_3 (*C*2/m) (the molar ratio of Ni, Co to Mn is the same as that in NCM 111). The core–shell structure of these LLOs was confirmed by XRD, TEM, and XPS. The Rietveld refinement data showed that these LLOs possess less Li^+/Ni^{2+} cation disorder and stronger M*–O (M* = Mn, Co, Ni) bonds than NCM 111. The core–shell material $Li_{1.15}Na_{0.5}(Ni_{1/3}Co_{1/3})_{core}(Mn_{1/3})_{shell}O_2$ can be cycled to a high upper cutoff potential of 4.7 V, delivers a high discharge capacity of 218 mAh g^{-1} at 20 mA g^{-1}, and retains 90 % of its discharge capacity at 100 mA g^{-1} after 90 cycles; thus, the use of this material in lithium ion batteries could substantially increase their energy density.

Keywords NCM 111 · Core–shell structure · Li_2MnO_3 · Cathode materials · Lithium ion battery · Energy density

✉ Lixu Lei
lixu.lei@seu.edu.cn

[1] School of Chemistry and Chemical Engineering, Southeast University, Nanjing 211189, China

[2] Department of Chemistry, College of Science, University of Karbala, Karbala 56001, Iraq

[3] Shenzhen Optimumnano Energy Co., Ltd., Shenzhen 518118, China

Introduction

$LiCoO_2$ is the traditional positive-electrode material for lithium ion batteries. However, its low energy density and high cost are currently driving a search for more efficient, economic, and stable materials for use in lithium ion batteries [1–4]. Doping with transition metals such as Mn and Ni has been the main focus of research in this field over the last few decades; an example of a useful doped material of this kind is $Li[Ni_{1/3}Co_{1/3}Mn_{1/3}]O_2$ (NCM 111). However, NCM 111 can only deliver a capacity of ~155 mAh g^{-1}, which is rather low if it is to be used in batteries for next-generation electric vehicles (EVs). Also, cycling this material at an upper cutoff potential >4.5 V causes the capacity to rapidly fade due to phase transitions from a rhombohedral structure to H1-3 and O1 phases [5–10].

Sakaebe et al. tested $LiNi_{1/3}Co_{1/3}Mn_{1/3}O_2$ at various upper cutoff potentials ranging from 4.5 to 4.9 V and found that the discharge capacity increased with increasing upper cutoff potential, but increasing the upper cutoff potential also led to a fast decline in capacity. They attributed this rapid drop in capacity to polarization caused by increased charge-transfer resistance (R_{ct}), indicating degradation of the interface between the electrode and electrolyte. The increase in polarization and R_{ct} can be effectively suppressed by applying an Al oxide coating, as this inhibits the formation of a rock-salt-structured phase in the surface region of bare NCM 111 during cycling [11].

Thackeray et al. proposed a new strategy to improve the stability of $LiMO_2$ materials by using Li_2MnO_3. They reported that preparing lithium-rich layered oxide materials (LLOs) xLi_2MnO_3–$(1-x)LiMO_2$ can yield high electrochemical capacities of ~250 mAh g^{-1} when charged to high potentials of >4.6 V, and they also reported that Li_2MnO_3 plays a major role in structural stability during the charge–discharge process. However, cycling this material at a high upper cutoff potential

of >4.6 V still resulted in an irreversible loss of capacity during the initial charge/discharge cycle and damaged the surface of the electrode, leading to high cell impedance [12, 13]. To overcome this issue, Kim et al. created a fluorine-substituted variant of $0.3Li_2MnO_3$–$0.7Li[Mn_{0.60}Ni_{0.25}Co_{0.15}]O_2$, treated the resulting material with acid, and then analyzed the electrochemical performance of this material. Their results showed that the pristine material delivered a discharge capacity of ~200 mAh g^{-1} at 0.5 C and retained 85 % of its capacity after 30 cycles in the potential range 2~4.6 V, while the surface-modified and fluorine-doped material retained 92 % of its capacity when cycled under the same conditions [14]. Thus, the surface treatment appeared to improve the stability of the material. Nevertheless, it retained only 93 % of its capacity after 30 cycles in the potential range 2~4.6 V. Therefore, LLOs with improved cycling stability and energy density (achieved by cycling them at higher upper cutoff potentials) are still required.

We recently reported a series of materials of formula $[Li_{1.2-x}Na_xNi_{0.62}Co_{0.14}Mn_{0.248}O_2]$, where $x = 0$, 0.05, 0.08, 0.10, and 0.12. Our results showed that coating an LLO with manganese oxide greatly enhanced its cycling stability and suppressed side reactions with the electrolytes. Sodium doping increases the lattice parameter *c* due to the fact that Na has a larger ionic radius than Li. This facilitates the diffusion of Li ions, reduces charge-transfer resistance, and improves the electrochemical performance of the materials [15].

Herein, we describe a new approach that allowed us to successfully synthesize an LLO material with high energy density and high stability, xLi_2MnO_3–$(1-x)LiMO_2$, a core–shell material in which the core is $LiMO_2$ and the shell is Li_2MnO_3. Thus, the aims of this study were (1) to increase the discharge capacity of NCM 111 by preparing NCM 111 with the formula xLi_2MnO_3–$(1-x)LiMO_2$, i.e., a lithium-rich material with a high capacity [12], and (2) to improve the thermal stability of this material by making it a core–shell structured material with a core of $LiMO_2$ and a shell of Li_2MnO_3. In this structure, Li_2MnO_3 has two advantages: it can participate in the electrochemical reactions at potentials >4.5 V, resulting in higher capacities, and it can increase the structural and thermal stability of the material during the charge–discharge process [14, 16, 17].

Experimental section

Materials and methods

$Ni_{0.5}Co_{0.5}CO_3$ was synthesized by a co-precipitation method in which $NiSO_4{\cdot}6H_2O$ and $CoSO_4{\cdot}7H_2O$ at a molar ratio of 1:1 were dissolved in deionized water to prepare a 1 M solution, which was then added to a 2 M Na_2CO_3 solution to form a suspension. This was aged for 12 h under a flow of N_2, with the temperature and pH of the solution maintained at 60 °C and 11, respectively. The suspension was filtered, washed, and dried in vacuum at 60 °C.

The core–shell material was prepared as follows. 0.528 g of $MnSO_4{\cdot}H_2O$ were dissolved in 50 ml of deionized water and added to 100 ml of an aqueous suspension containing 0.5 g of the precursor $Ni_{0.5}Co_{0.5}CO_3$ and 0.4 g of Na_2CO_3. Aging was performed for 12 h at 60 °C. The resultant suspension was filtered, washed three times with deionized water, and dried in a vacuum at 60 °C.

$Li_{1.15}Na_{0.5}(Ni_{1/3}Co_{1/3})_{core}(Mn_{1/3})_{shell}O_2$ was obtained by mixing a stoichiometric amount of the precursor with appropriate amounts of Li_2CO_3 and Na_2CO_3. The mixed powder was first heated at 450 °C for 8 h, followed by sintering at 900 °C for 12 h in air. The heating rate was maintained at 2 °C min^{-1}.

The pristine $LiNi_{1/3}Co_{1/3}Mn_{1/3}O_2$ material was synthesized by a co-precipitation method. Stoichiometric amounts of $NiSO_4{\cdot}6H_2O$, $CoSO_4{\cdot}7H_2O$, and $MnSO_4{\cdot}H_2O$ were dissolved in deionized water in which the total concentration of metals was 1 M; this was denoted solution A. Solution A was added to a 2 M Na_2CO_3 solution under vigorous stirring and then aged for 12 h under an N_2 atmosphere. The temperature and pH of the solution were maintained at 60 °C and 11, respectively. The resultant suspension was filtered, washed, and dried in a vacuum at 60 °C. $LiNi_{1/3}Co_{1/3}Mn_{1/3}O_2$ was obtained by mixing stoichiometric powder of the precursor with an appropriate amount of Li_2CO_3. The mixture was first heated at 450 °C for 8 h and then baked at 900 °C for 12 h in air. The heating rate was maintained at 2 °C min^{-1}.

Physical characterization

Powder X-ray diffraction was accomplished on a Shimadzu XD-3A diffractometer using Cu K_α radiation (λ = 0.15406 nm), at a scan rate of 0.15° 2θ min^{-1} with a step size of 0.02° in the 2θ range 10–80°.

Transmission electron microscopy (TEM) was performed on a JEM2000EX (JEOL, Tokyo, Japan) transmission electron microscope. The morphology was observed using a scanning electron microscope (SEM, FESEM, SU8010, Hitachi, Tokyo, Japan). The electrode was prepared as follows. The synthesized material was mixed with acetylene carbon black (AB) and poly(vinylidene fluoride) (PVDF), weight ratio 80:10:10, and then dispersed in 1-methyl-2-pyrrolidinone (NMP). The resulting slurry was spread onto a disk of aluminum foil with a loading mass of 2~3 mg cm^{-2} and then dried in a vacuum oven at 65 °C for 24 h. CR 2032 coin cells were assembled in an Ar-filled glove box with a Li counter electrode and 1 M $LiPF_6$ dissolved in ethylene carbonate (EC) and dimethyl carbonate (DMC) used as the electrolyte. The cells were galvanostatically charged/discharged within the range 2.5~4.7 V at room temperature, while the pristine material was charged to an upper cutoff potential of 4.5 V. The cells were galvanostatically charged at different current densities to

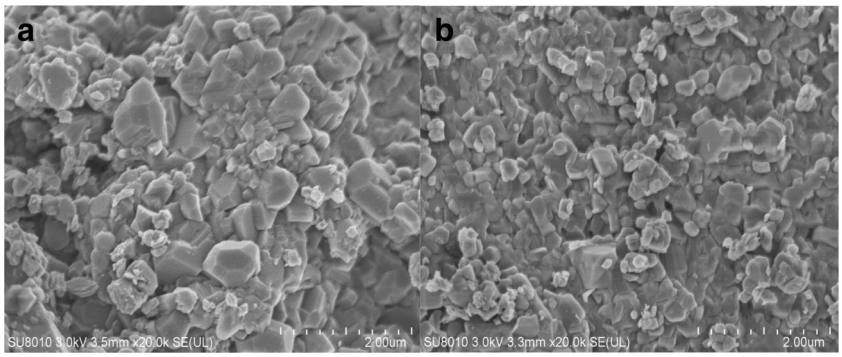

Fig. 1a–b SEM images of **a** the pristine material and **b** the core–shell material

4.7 V. This was followed by an additional constant-voltage (CV) charging step at 4.7 V until the current reached 70 % of the charge current, and then the cells were discharged galvanostatically to 2.5 V using a battery cycler (battery testing system, Land, Wuhan, China) at room temperature. The current densities used were 20, 100, 200, 400, 1000, and 2000 mA g^{-1}.

Results and discussion

The materials were synthesized by coprecipitating stoichiometric amounts of Ni^{2+} and Co^{2+} sulfates with Na_2CO_3 and aging for 12 h, during which the pH and temperature were maintained at 11 and 60 °C, respectively. The material was synthesized at a high pH to precipitate a higher percentage of cobalt from the solution. Furthermore, the surface of the synthesized material is partially negatively charged at high pH, aiding the creation of a homogeneous coating. The precursor was then coated with manganese oxide, as described in the "Experimental section." The precursor was mixed with appropriate amounts of Li_2CO_3 and Na_2CO_3 to produce the cathode material for LIBs. We doped the core–shell material with sodium to further improve its electrochemical performance. Previously, we reported that sodium doping can significantly enhance electrochemical performance, as it results in the expansion of the lattice parameter *c* [15].

Figure 1 shows SEM images of the core–shell and pristine materials. It can be seen that the particles of the core–shell material are smaller than those of the pristine material, which can be attributed to the longer aging period applied.

It can be seen that the core–shell material's primary particles are plate-like in shape and ~150 nm in size (Fig. 2a). The selected area electron diffraction (SAED) pattern (Fig. 2b) exhibits sets of lattice fringes with interplanar spacings of 0.470 nm, 0.233 nm, 0.171 nm, 0.155 nm, and 0.111 nm, which can be indexed to the $(003)_{R\text{-}3m}$ or $(001)_{C2/m}$, $(012)_{R\text{-}3m}$ or $(200)_{C2/m}$,

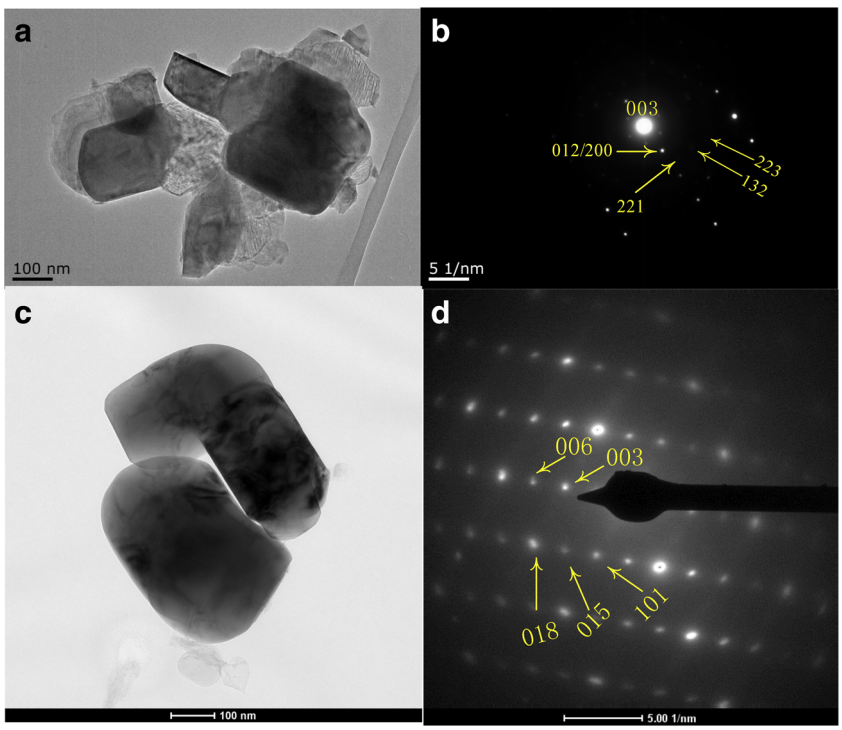

Fig. 2 **a** TEM image of the core–shell material, **b** electron diffraction pattern of the core–shell material, **c** TEM image of the pristine material, and **d** electron diffraction pattern of the pristine material

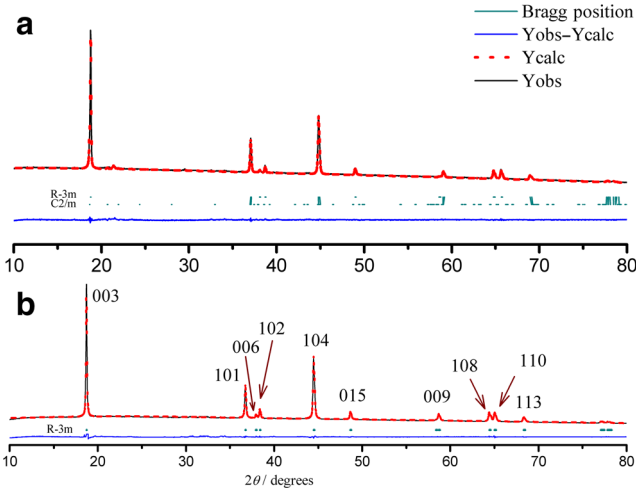

Fig. 3a–b Profiles for Rietveld refinement of the **a** core–shell and **b** pristine materials. *Red dots* indicate the calculated profile; *black solid line* indicates observed data; *green dots* indicate Bragg positions; *blue solid line* indicates ($Y_{obs} - Y_{calc}$)

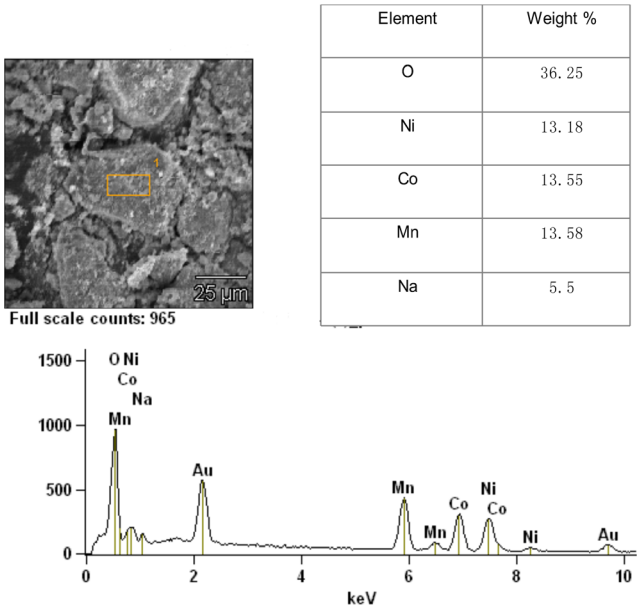

Fig. 4 EDS data on the core–shell-structured material

$(221)_{C2/m}$, $(132)_{C2/m}$, and $(223)_{C2/m}$ diffractions of either a trigonal (layered α-$NaFeO_2$ type, space group *R*-3m) or monoclinic (space group *C*2/m) structure, respectively (please refer to the XRD data for more information) [12, 18, 19]. This indicates that the core–shell material is heterostructured with *R*-3m and *C*2/m phases. The monoclinic Li_2MnO_3 (*C*2/m) is compatible with the trigonal $LiMO_2$ (*R*-3m) structure due to the fact that the *R*-3m and *C*2/m phases both possess interlayer spacing of 4.7 Å, which can be attributed to the 003 and 001 planes of the *R*-3m and *C*2/m phases, respectively [12] .

To further compare the structures of the pristine and core–shell materials, we characterized the pristine material using a high-resolution transmission electron microscope (HRTEM) (Fig. 2d and e). The pristine material's primary particles are also plate-like shape and 100~200 nm in size. The SAED pattern exhibits lattice fringes with spacings of 0.47, 0.235, 0.143, 0.186, and 0.243 nm, which can be indexed to the 003, 006, 018, 015, and 101 diffractions of the α-$NaFeO_2$-type structure (space group *R*-3m), respectively. These results indicate that the core–shell material is a mixture of layered (*R*-3m) and monoclinic *C*2/m phases, while the pristine material is a pure layered (*R*-3m) structure.

The XRD patterns and the profiles of Rietveld refinements are shown in Fig. 3. As discussed above, the Li_2MnO_3 (monoclinic *C*2/m) and $LiMO_2$ (trigonal *R*-3m) structures are compatible due to the fact that the interlayer spacing of the close-packed layers is ~4.7 Å for both structures, which can be attributed to the 003 and 001 planes of the *R*-3m and *C*2/m phases, respectively [12]. Note that the XRD data are often difficult to interpret uniquely for these two systems because all of the peaks for the *R*-3m structure can also be indexed to the *C*2/m structure. However, reflections that appear in the 2θ range ~20–23° (Cu Kα) can only be indexed to the monoclinic structure and are a signature of the $LiMn_6$ unit in the Li_2MnO_3 [20]. Therefore, the Rietveld refinements were carried out in this study by assuming that the core–shell material is a mixture of trigonal (*R*-3m) and monoclinic (*C*2/m) phases, while the pristine sample is a pure trigonal phase, because no sign of the *C*2/m phase in the 2θ range ~20–23° (Cu Kα) has been observed [12–14, 21].

For the trigonal (*R*-3m) phase, Li, a transition metal (Ni, Co, or Mn), and O occupy the 3a (0 0 1/2), 3b (0 0 0), and 6c (0 0 1/4) sites, respectively. The Ni^{2+}/Li^{+} disorder between the 3a and 3b sites is considered to be due to the similar ionic radii of the Ni^{2+} (0.76 Å) and Li^{+} (0.70 Å) ions [22, 23].

Some selected results of Rietveld refinements obtained using the Fullprof package [24] are listed in Table 1. Table 1 shows that the pristine material exhibits a pure *R*-3m phase, while the core–shell material is a mixture of *R*-3m and *C*2/m phases. Table 1 also shows that the M*–O bonds (M* = Ni, Mn, Co) of the core–shell material are stronger than those of the pristine material. This should result in increased structural stability, decreased oxygen release during charge/discharge processes, and reduced Ni^{2+} migration to Li slab because it makes vacancy formation in the transition metal layer more difficult [25].

Table 1 Results of Rietveld refinement for the synthesized materials

Sample	Ni^{2+} in Li layer (%)	*a*-axis (Å)	*c*-axis (Å)	Li–O (Å)	M*–O (Å)	R_{wp} (%)	*R*-3m, phase%	*C*2/m, phase%
Pristine	2.91	2.840	14.225	2.089	1.980	5.3	100	0
Core–shell	1.96	2.838	14.215	2.103	1.975	4.9	41	59

Table 2 Electron-density distributions of the synthesized samples

Sample	Position	*x/a*	*y/b*	*z/c*	Electron density
Pristine	Li site	0	0	1/2	22.7
	Metal site	0	0	0	196.4
Core–shell	Li site	0	0	1/2	20.2
	Metal site	0	0	0	198.3

Figure 4 shows SEM-EDS data on the core–shell structure. It indicates that the actual chemical composition of the material is very similar to the proposed composition.

XRD data were employed to determine the electron-density distributions in the pristine and core–shell materials using the Fullprof package. The results (Table 2) show that the electronic density at the Li site (0 0 1/2) is lower in the core–shell material, which can be ascribed to the decreased amount of Ni^{2+} in the Li layer.

The fits of the Ni 2*p* orbital peaks to the XPS spectra of the pristine and core–shell materials are shown in Fig. 5. Since the binding energy of the Ni(III) 2*p* orbitals is higher than that of Ni(II), it is possible to calculate the Ni^{3+} and Ni^{2+} contents of the synthesized materials. The results show that the Ni^{2+} content of the core–shell material is more than that of the pristine material. This increase in Ni^{2+} may arise because some of the Mn^{4+} from the Li_2MnO_3 shell interdiffuses into the surface of the core material and Ni^{2+} from the core material diffuses into the shell, which causes the core and the shell to fuse together. This fusion definitely increases the chemical and thermal stability of the material.

Electrochemical performance

Figure 6 displays the initial charge–discharge profiles of the samples at 20 mA g^{-1} and different cutoff potentials. We charged the pristine sample to an upper cutoff potential of 4.5 V because potentials higher than this can lead to a rapid decrease in capacity and structural collapse [11], while the core–shell material could be cycled to an upper cutoff potential of 4.7 V with high stability.

The pristine sample delivers an initial discharge capacity of 168 mAh g^{-1} at 20 mA g^{-1}, while the core–shell material delivers 208 mAh g^{-1} at the same current density (Fig. 6). This shows that the core–shell structured material delivers a much higher discharge capacity than the pristine material, because LLOs can deliver a high discharge capacity when cycled at an upper cutoff potential of >4.5 V [12–14, 16, 17, 20, 21, 26, 27].

It can be seen that the core–shell material operates at a much higher potential than the pristine material (Fig. 6). The discharge capacity of the core–shell structured material increased to 218 mAh g^{-1} after cycling for four cycles, due to the electrochemical activation of the Li_2MnO_3 phase (Fig. 7) [16, 28].

The pristine and core–shell materials deliver discharge capacities of 203.4 and 155.2 mAh g^{-1} at a current density of 100 mA g^{-1}, and retain 79 and 90 % of their peak capacities after 90 cycles at room temperature, respectively (Fig. 7). This high stability of the core–shell structure can be attributed to the Li_2MnO_3-phase shell and stronger M^*–O bonds (as mentioned earlier in the discussion of the XRD analysis results), which can provide high structural stability in the highly delithiated state [12, 13, 28].

To further investigate the differences between the pristine and core–shell materials, we also tested the half-cells at different current densities (Fig. 8). The core–shell material delivered the highest discharge capacity of 218 mAh g^{-1} at 20 mA g^{-1}, which was much higher than that of a recently reported material [11]. For example, Xia et al. reported that a solid solution of $LiNi_{0.8}Co_{0.1}Mn_{0.1}O_2$ and Li_2MnO_3 which was cycled at an upper cutoff potential of 4.5 V delivered a discharge capacity of 207 mAh g^{-1} and retained 75 % of its capacity after 100 cycles at 20 mA g^{-1} [29]. Moreover, the core–shell material synthesized in this study exhibited a higher discharge capacity than the pristine material and better stability than it at all current densities (Fig. 8).

The average discharge potential is highly dependent on the discharge profile [30]. In $LiMO_2$ materials, voltage fading is a serious issue because voltage fading results in

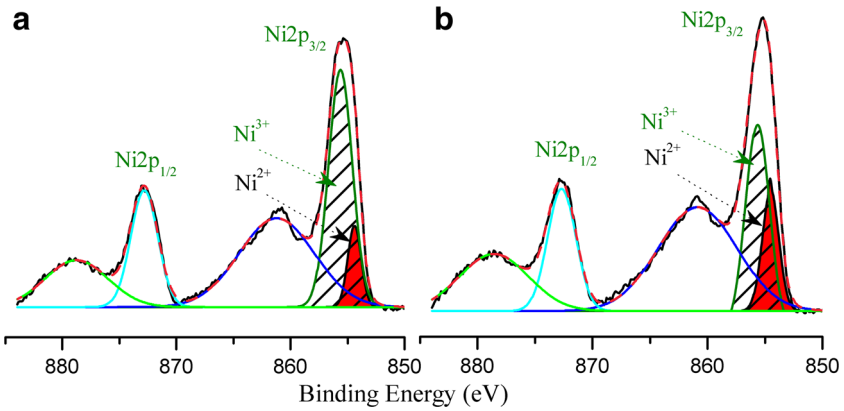

Fig. 5a–b XPS spectra of the **a** pristine and **b** core–shell structured materials

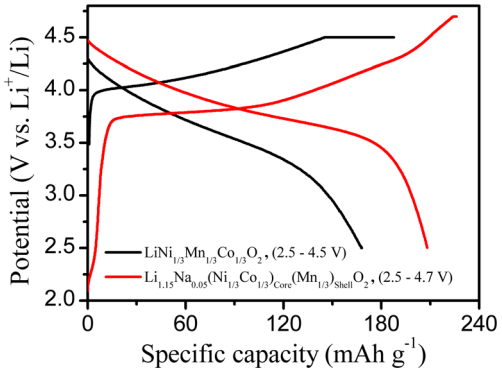

Fig. 6 Initial charge–discharge profiles of the pristine and core–shell structured materials at 20 mA g^{-1}

a dramatic decrease in energy density, even though discharge capacity fading can be prevented [24–29]. Figure 9 compares the average potential profiles of the core–shell and pristine materials, and shows that the core–shell material operates at much higher potential than the pristine material, with less potential fading upon cycling. This indicates that the presence of the Li_2MnO_3 shell significantly increases the energy density and improves structural stability [16, 29, 31, 32].

Cyclic voltammetry was also carried out to study the differences between the pristine and core–shell materials (Fig. 10). The prepared cells were scanned anodically, followed by a corresponding cathodic scan. A couple of redox peaks were observed for both samples. The anodic peaks located in the potential range 4–4.2 V can be attributed to the redox couple of Ni^{2+} and Co^{3+} [33].

The core–shell material displays a broad oxidation peak with a higher current than the pristine material. In addition, one more reduction peak (at ~3 V) was observed for the core–shell material, which can be attributed to the Mn^{3+}/Mn^{4+} redox couple; this could explain the increased capacity shown by this material [17].

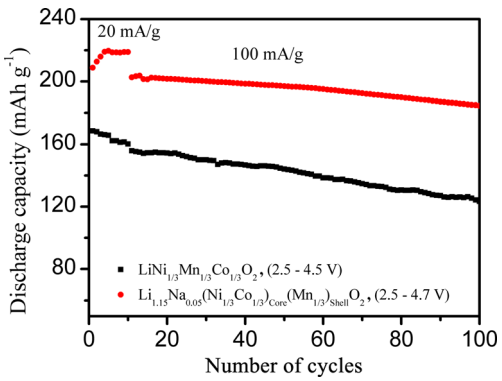

Fig. 7 Cycling performances of the pristine and core–shell structured materials at 20 mA g^{-1} for 10 cycles, followed by 90 cycles at 100 mA g^{-1}. The pristine sample was cycled between 2.5 and 4.5 V, while the core–shell sample was cycled between 2.5 and 4.7 V

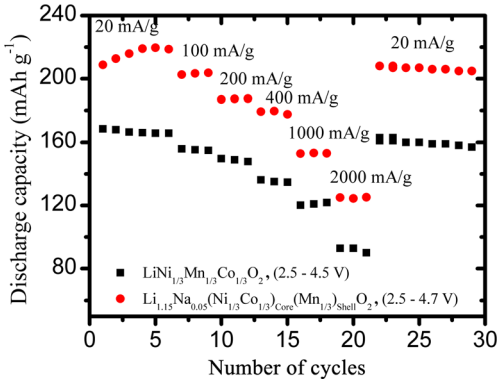

Fig. 8 Rate capability performances at different current densities of the pristine and core–shell structured materials at room temperature. The pristine sample was cycled between 2.5 and 4.5 V, while the core–shell sample was cycled between 2.5 and 4.7 V

Conclusions

$Li_{1.15}Na_{0.5}(Ni_{1/3}Co_{1/3})_{core}(Mn_{1/3})_{shell}O_2$ was successfully synthesized via coprecipitation and subsequent baking at 900 °C for 12 h in air. Using XRD, TEM, and XPS, we confirmed the structure of this material. The core–shell material is composed of a core of a layered $LiMO_2$ phase (*R*-3m), while the shell is a monoclinic Li_2MnO_3 phase (*C*2/m).

Rietveld refinements show that the core–shell structured material has less Li^+/Ni^{2+} cation disorder than the pristine material. They also reveal that stronger M*–O (M* = Mn, Co, Ni) bonds are present in the core–shell material, which leads to high structural stability during the charge–discharge process.

The core–shell material can be cycled at a higher upper cutoff potential of 4.7 V than that of the pristine material (4.5 V). Therefore, it can be concluded that the presence of the Li_2MnO_3 shell substantially improves the electrochemical performance of the material in terms of its discharge capacity, energy density, and cycling stability. $Li_{1.15}Na_{0.5}(Ni_{1/3}Co_{1/3})_{core}(Mn_{1/3})_{shell}O_2$

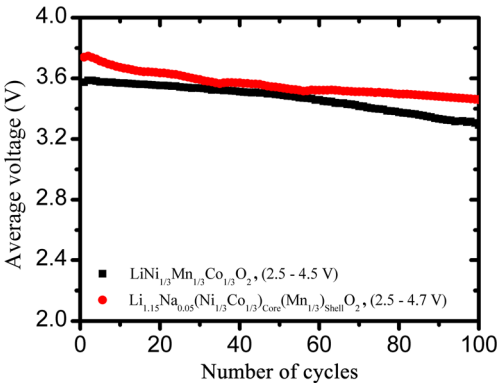

Fig. 9 Average voltage vs. number of cycles for the core–shell and pristine materials at a current density of 20 mA g^{-1} for 10 cycles followed by 90 cycles at 100 mA g^{-1}. The pristine sample was cycled between 2.5 and 4.5 V, while the core–shell sample was cycled between 2.5 and 4.7 V

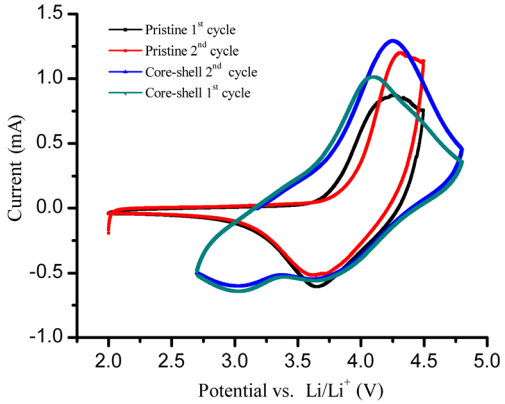

Fig. 10 Cyclic voltammograms of the pristine and core–shell structured materials

delivers a high discharge capacity of 218 mAh g^{-1} at 20 mA g^{-1} and retains 90 % of its discharge capacity at 100 mA g^{-1} after 90 cycles at 100 mA g^{-1}. This discharge capacity is much higher than that of the classic NCM 111 material. The core–shell material displays a higher average voltage, a higher energy density, and better cycling stability than those of the pristine material.

References

1. Santhanam R, Rambabu B (2010) Research progress in high voltage spinel $LiNi_{0.5}Mn_{1.5}O_4$ material. J Power Sources 195(17): 5442–5451
2. Han S, Xia Y, Wei Z, Qiu B, Pan L, Gu Q, Liu Z, Guo Z (2015) A comparative study on the oxidation state of lattice oxygen among $Li_{1.14}Ni_{0.136}Co_{0.136}Mn_{0.544}O_2$, Li_2MnO_3, $LiNi_{0.5}Co_{0.2}Mn_{0.3}O_2$ and $LiCoO_2$ for the initial charge–discharge. J Mater Chem A 3(22): 11930–11939
3. Dou S (2013) Review and prospect of layered lithium nickel manganese oxide as cathode materials for Li-ion batteries. J Solid State Electrochem 17(4):911–926
4. Kim H-S, Kim K, Moon S-I, Kim I-J, Gu H-B (2008) A study on carbon-coated $LiNi_{1/3}Mn_{1/3}Co_{1/3}O_2$ cathode material for lithium secondary batteries. J Solid State Electrochem 12(7–8):867–872
5. Van der Ven A, Aydinol MK, Ceder G (1998) First-principles evidence for stage ordering in Li_xCoO_2. J Electrochem Soc 145(6): 2149–2155
6. Jiang X, Sha Y, Cai R, Shao Z (2015) The solid-state chelation synthesis of $LiNi_{1/3}Co_{1/3}Mn_{1/3}O_2$ as a cathode material for lithium-ion batteries. J Mater Chem A 3(19):10536–10544
7. Noh H-J, Youn S, Yoon CS, Sun Y-K (2013) Comparison of the structural and electrochemical properties of layered $Li[Ni_xCo_yMn_z]O_2$ ($x = 1/3$, 0.5, 0.6, 0.7, 0.8 and 0.85) cathode material for lithium-ion batteries. J Power Sources 233:121–130
8. Xia H, Lu L, Meng YS, Ceder G (2007) Phase transitions and high-voltage electrochemical behavior of $LiCoO_2$ thin films grown by pulsed laser deposition. J Electrochem Soc 154(4):A337
9. Lin B, Wen Z, Wang X, Liu Y (2010) Preparation and characterization of carbon-coated $Li[Ni_{1/3}Co_{1/3}Mn_{1/3}]O_2$ cathode material for lithium-ion batteries. J Solid State Electrochem 14(10):1807–1811
10. Yang S, Wang X, Yang X, Liu L, Liu Z, Bai Y, Wang Y (2011) Influence of Li source on tap density and high rate cycling performance of spherical $Li[Ni_{1/3}Co_{1/3}Mn_{1/3}]O_2$ for advanced lithium-ion batteries. J Solid State Electrochem 16(3):1229–1237
11. Yano A, Aoyama S, Shikano M, Sakaebe H, Tatsumi K, Ogumi Z (2015) Surface structure and high-voltage charge/discharge characteristics of Al-oxide coated $LiNi_{1/3}Co_{1/3}Mn_{1/3}O_2$ cathodes. J Electrochem Soc 162(2):A3137–A3144
12. Thackeray MM, Kang S-H, Johnson CS, Vaughey JT, Benedek R, Hackney SA (2007) Li_2MnO_3-stabilized $LiMO_2$ (M = Mn, Ni, Co) electrodes for lithium-ion batteries. J Mater Chem 17(30):3112–3125
13. Kang SH, Thackeray MM (2008) Stabilization of $xLi_2MnO_3{\cdot}(1-x)LiMO_2$ electrode surfaces (M = Mn, Ni, Co) with mildly acidic, fluorinated solutions. J Electrochem Soc 155(4):A269
14. Kim S-M, Jin B-S, Lee S-M, Kim H-S (2015) Effects of the fluorine-substitution and acid treatment on the electrochemical performances of $0.3Li_2MnO_3 \cdot 0.7LiMn_{0.60}Ni_{0.25}Co_{0.15}O_2$ cathode material for Li-ion battery. Electrochim Acta 171:35–41
15. Mezaal MA, Qu L, Li G, Zhang R, Jiang X, Zhang K, Liu W, Lei L (2015) Promoting the cyclic and rate performance of lithium-rich ternary materials via surface modification and lattice expansion. RSC Adv 5(113):93048–93056
16. Li J, Xu Y, Li X, Zhang Z (2013) Li_2MnO_3 stabilized $LiNi_{1/3}Co_{1/3}Mn_{1/3}O_2$ cathode with improved performance for lithium ion batteries. Appl Surf Sci 285:235–240
17. Yu H, Zhou H (2013) High-energy cathode materials (Li_2MnO_3-$LiMO_2$) for lithium-ion batteries. J Phys Chem Lett 4(8):1268–1280
18. Yang C, Zhang Q, Ding W, Zang J, Lei M, Zheng M, Dong Q (2015) Improving the electrochemical performance of layered lithium-rich cathode materials by fabricating a spinel outer layer with Ni^{3+}. J Mater Chem A 3(14):7554–7559
19. Yan J, Liu X, Li B (2014) Recent progress in Li-rich layered oxides as cathode materials for Li-ion batteries. RSC Adv 4(108):63268–63284
20. Long BR, Croy JR, Dogan F, Suchomel MR, Key B, Wen J, Miller DJ, Thackeray MM, Balasubramanian M (2014) Effect of cooling rates on phase separation in $0.5Li_2MnO_3{\cdot}0.5LiCoO_2$ electrode materials for Li-ion batteries. Chem Mater 26(11):3565–3572
21. Son MY, Lee JK, Kang YC (2014) Fabrication and electrochemical performance of $0.6Li_2MnO_3$-$0.4Li(Ni_{1/3}Co_{1/3}Mn_{1/3})O_2$ microspheres by two-step spray-drying process. Sci Rep 4:5752
22. Park MS (2014) First-principles study of native point defects in $LiNi_{1/3}Co_{1/3}Mn_{1/3}O_2$ and Li_2MnO_3. Phys Chem Chem Phys 16(31):16798–16804
23. Kumar PS, Sakunthala A, Reddy MV, Shanmugam S, Prabu M (2015) Correlation between the structural, electrical and electrochemical performance of layered $Li(Ni_{0.33}Co_{0.33}Mn_{0.33})O_2$ for lithium ion battery. J Solid State Electrochem 20(7):1665–1876
24. Boultif A, Louër D (2004) Powder pattern indexing with the dichotomy method. J Appl Crystallogr 37(5):724–731
25. Liu W, Oh P, Liu X, Lee MJ, Cho W, Chae S, Kim Y, Cho J (2015) Nickel-rich layered lithium transition-metal oxide for high-energy lithium-ion batteries. Angew Chem Int Ed Engl 54(15):4440–4457
26. Oh P, Ko M, Myeong S, Kim Y, Cho J (2014) A novel surface treatment method and new insight into discharge voltage deterioration for high-performance $0.4Li_2MnO_3$-$0.6LiNi_{1/3}Co_{1/3}Mn_{1/3}O_2$ cathode materials. Adv Energ Mater 4(16):1400631
27. Noh JK, Kim S, Kim H, Choi W, Chang W, Byun D, Cho BW, Chung KY (2014) Mechanochemical synthesis of Li_2MnO_3 shell/$LiMO_2$ (M = Ni, Co, Mn) core-structured nanocomposites for lithium-ion batteries. Sci Rep 4:4847
28. Ryu W-H, Kim D-H, Kang S-H, Kwon H-S (2013) Electrochemical properties of nanosized Li-rich layered

oxide as positive electrode materials for Li-ion batteries. RSC Adv 3(22):8527–8534
29. Yang J, Hou M, Haller S, Wang Y, Wang C, Xia Y (2016) Improving the cycling performance of the layered Ni-rich oxide cathode by introducing low-content Li_2MnO_3. Electrochim Acta 189:101–110
30. Li Q, Li G, Fu C, Luo D, Fan J, Xie D, Li L (2015) Balancing stability and specific energy in Li-rich cathodes for lithium ion batteries: a case study of a novel Li–Mn–Ni–Co oxide. J Mater Chem A 3(19):10592–10602
31. Fu F, Deng Y-P, Shen C-H, Xu G-L, Peng X-X, Wang Q, Xu Y-F, Fang J-C, Huang L, Sun S-G (2014) A hierarchical micro/nanostructured $0.5Li_2MnO_3{\cdot}0.5LiMn_{0.4}Ni_{0.3}Co_{0.3}O_2$ material synthesized by solvothermal route as high rate cathode of lithium ion battery. Electrochem Commun 44:54–58
32. Shen CH, Huang L, Lin Z, Shen SY, Wang Q, Su H, Fu F, Zheng XM (2014) Kinetics and structural changes of Li-rich layered oxide $0.5Li_2MnO_3.0.5LiNi_{0.292}Co_{0.375}Mn_{0.333}O_2$ material investigated by a novel technique combining in situ XRD and a multipotential step. ACS Appl Mater Interfaces 6(15):13271–13279
33. Li W, Reimers J, Dahn J (1992) Crystal structure of $Li_xNi_{2-x}O_2$ and a lattice-gas model for the order–disorder transition. Phys Rev B 46(6):3236–3246